Covalency-driven structural instability and spin-phonon coupling in barium cobalt oxychloride

Tanushree Chakraborty,[1] S. Baidya,[2] Carlo Meneghini,[3,*] Tanusri Saha-Dasgupta,[2,†] Giulia Veronesi,[4] Marco Merlini,[5] Hiroko Yokota,[6] Mitsuru Itoh,[7] S. Majumdar,[8] and Sugata Ray[1,9,‡]

[1]*Centre for Advanced Materials, Indian Association for the Cultivation of Science, Jadavpur, Kolkata 700032, India*
[2]*Department of Condensed Matter and Materials Science, S. N. Bose National Centre for Basic Sciences, JD Block, Sector III, Salt Lake, Kolkata 700098, India*
[3]*Dipartimento di Scienze, Universitá Roma Tre, Via della Vasca Navale, 84 I-00146 Roma, Italy*
[4]*European Synchrotron Radiation Facility, POB 220, Grenoble Cedex 9, France*
[5]*Università di Milano–Dip. di Scienze della Terra Ardito Desio, Milano, Italy*
[6]*Department of Physics, Chiba University, 1-33 Yayoi-cho, Inage-ku, Chiba 263-8522, Japan*
[7]*Materials and Structures Laboratory, Tokyo Institute of Technology, 4259 Nagatsuta, Yokohama 226-8503, Japan*
[8]*Solid State Physics, Indian Association for the Cultivation of Science, Jadavpur, Kolkata 700032, India*
[9]*Department of Materials Science, Indian Association for the Cultivation of Science, Jadavpur, Kolkata 700032, India*

(Received 2 July 2014; revised manuscript received 1 December 2014; published 29 December 2014)

Our combined experimental and theoretical study reveals unusually large cobalt-oxygen covalency in CoO_4 tetrahedral unit of a barium cobalt oxychloride compound. This drives significant charge redistribution, resulting into large hole density on tetrahedral oxygens, which effectively behave as "*positively charged*" anions. These *positively charged* oxygens form local dipoles with dopant chloride anions, situated in the same atomic plane, which gets manifested in associated structural distortions. The spatial freezing of these local dipoles below certain temperature is found to produce concomitant effects on dielectric and magnetic responses, coupled via exchange-striction driven spin-phonon interaction. Our study should form the basis for designing new functional oxide materials using the concept of covalency-driven charge redistribution.

DOI: 10.1103/PhysRevB.90.235147 PACS number(s): 72.80.Ga, 61.05.cj, 71.15.Mb, 77.22.Ch

I. INTRODUCTION

According to the Zaanen-Sawatzky-Allen phase diagram [1,2], the late 3*d* transition metal (TM) oxide insulators for which the charge-transfer energy is smaller compared to the Coulomb correlation, are charge-transfer insulators, as opposed to the Mott-Hubbard insulators. A crucial variable for these compounds, as discussed recently, is the number of *d* electrons, a parameter which gets strongly influenced by the metal-oxygen covalency [3]. Unusually large metal-oxygen covalency, leading to significant changes in the *d* electron count at the TM site has been discussed in literature. One most spectacular example is that of $KMnO_4$ [4–7], in which the formal charge of +7 on Mn effectively reduces to about +2 due to massive redistribution of electronic charges, following large metal-oxygen covalency. It has been observed that such covalency driven charge redistribution is more preferred within a metal-oxygen tetrahedron than in an octahedral unit [8–11]. Therefore, simultaneous presence of tetrahedral and octahedral motifs in a unit cell may provoke different types of charge distributions at different parts of the unit cell. This can further be escalated by creation of irregularities within the anionic network via anion doping. Introduction of dissimilar anions having different electronegativity, charge, and electronic polarizablility is expected to tune the valence states of cations, the bond covalency, and even the structural symmetry. All these effects can individually or collectively drive certain instability(s) in the system and consequently give rise to interesting functionality.

In the present study, we explore these possibilities in an oxychloride compound, $Ba_5Co_5ClO_{13}$ (BCCO5) [12–17], which possesses (a) octahedral as well as tetrahedral Co-O units, and (b) chemical substitution of oxygen by chlorine. This compound was first reported by Yamamura *et al.* [12] as an antiferromagnetic insulator. Later, the work by Mentre *et al.* [15] and Wang *et al.* [13] provided details of this antiferromagnetic structure. However, the most curious issue concerning the structure is the unusual site instability of one particular oxygen ion in the structure [16], which, though mentioned, has not been investigated in detail. Importantly, the correlation between the large cobalt-oxygen covalency within the CoO_4 tetrahedra and the structural instability in this compound, and its possible role in driving new functionalities, has not been studied before.

In this study, we exploited spectroscopic tools like x-ray absorption fine structure (XAFS) spectroscopy in near-edge (XANES) and extended region (EXAFS) to investigate the local structural and electronic properties, combined with measurement of dielectric and magnetic properties, and *ab initio* density functional theory based calculations. Our study shows signature of unusual tetrahedral Co-O covalency driven hole density on oxygen site, which together with engineered irregularities in the anionic network, triggers two important effects: (i) formation of Cl-O local dipoles and a consequent giant dielectric constant and (ii) activation of spin-phonon coupling via exchange striction.

II. EXPERIMENTAL AND THEORETICAL DETAILS

$Ba_5Co_5ClO_{13}$ single crystals were grown by flux method following earlier reports [17]. $Ba_5Co_5ClO_{13}$ polycrystalline powders were prepared by a solid state reaction method by

*carlo.meneghini@uniroma3.it
†t.sahadasgupta@gmail.com
‡mssr@iacs.res.in

taking the stoichiometric quantities of dried $BaCO_3$, Co_3O_4, and $BaCl_2$. At first the precursors were homogeneously ground in a mortar with ethanol and calcined at 1000 °C for 10 h in air and then quenched to room temperature. The phase purity of the sample was checked by powder XRD in a Bruker AXS: D8 Advanced diffractometer equipped with Cu K_α radiation. Cl K-edge (2.822 keV) polarized XAFS measurements (p-XAFS) were carried out on a small ($0.25 \times 0.5 \times 0.5$ mm^3) $Ba_5Co_5ClO_{13}$ single crystal in fluorescence geometry at the ESRF-ID21 beamline using a small (about 13 μm) x-ray beam, linearly polarized in the horizontal plane. The direction specific spectra were collected in the XANES region orienting the BCCO5 crystal in ways such that z-, x-, and y-crystallographic directions lie along the x-ray polarization axis ϵ in different measurements. The analysis of the p-XANES spectra were carried out comparing the experimental data with *ab initio* simulations calculated using FEFF8 program [18], where full multiple scattering theory is employed on a local cluster of 8 Å around the absorber. Cl K-edge EXAFS for the polycrystalline powder was collected at the ELETTRA (Trieste, Italy) synchrotron radiation facility (XAFS beamline) in fluorescence geometry. Data treatment and quantitative analysis in the extended (EXAFS) region was carried out using ESTRA and FITEXA programs [27]. FEFF program [18] was used to calculate theoretical amplitude and phase functions from representative atomic clusters obtained based on the $Ba_5Co_5ClO_{13}$ crystallographic structure. The Co K-edge (7.709 keV) measurements were restricted to the near edge region (XANES) of the absorption spectra to understand the average Co electronic state (Fig. 2). The XPS measurements were carried out on an annealed pellet of BCCO5 in an Omicron electron spectrometer, equipped with EA125 analyzer and Mg K_α x-ray source. The dielectric and specific heat measurements were carried out in a Quantum Design PPMS in Tokyo Institute of Technology, Japan. Dielectric measurements were carried out on single crystals, on which metal electrodes were deposited on the *ab* plane and thin Pt wires were connected using Ag paste. The magnetization behavior along different directions was measured in a Quantum Design SQUID magnetometer in Chiba University, Japan.

We calculated the electronic and magnetic properties of BCCO5 using first principles density functional theory (DFT). For the DFT calculations we have primarily used the plane wave basis set and pseudopotentials as implemented in the Vienna Ab-initio Simulation Package (VASP) [19]. The exchange-correlation function was chosen to be that of the generalized gradient approximation (GGA) implemented following the parametrization of Perdew-Burke-Ernzerhof [20]. The electron-electron correlation beyond GGA was taken into account through improved treatment of GGA+U calculation within the +U implementation of Dudarev *et al.* [21]. For the plane-wave based calculations, we used projector augmented wave (PAW) [22] potentials. A U value of 4 eV with $J_H = 0.8$ eV on Co site was used. The obtained results were verified in terms of variation of U parameter. To check the validity of plane-wave results, full-potential linearized augmented plane-wave (FLAPW) calculations as implemented [23] in WIEN2K were carried out. For FLAPW calculations, we chose the APW+lo as the basis set and the expansion in spherical harmonics for the radial wave functions was taken up to $l = 10$. The charge densities and potentials were represented by spherical harmonics up to $l = 6$. To calculate IR active phonons we carried out density functional perturbation theory (DFPT) [24] as implemented in VASP. The method involves direct computation of the second derivative of the total energy. For our purpose, we calculated the dynamical matrix at Γ point in the BZ.

III. RESULTS AND DISCUSSIONS

Crystal structure. The hexagonal unit cell of $Ba_5Co_5ClO_{13}$ is shown in Fig. 1(a). Figure 1(b) shows the x-ray diffraction (XRD) pattern of BCCO5 which confirms phase purity of the sample. The structure consists of chainlike motifs running along crystallographic c direction, made up of three face-sharing CoO_6 octahedral units [Co(1) and Co(2)], connected to the next unit via a pair of corner-shared CoO_4 tetrahedra [Co(3)]. Unlike parent 5H-$Ba_5Co_5O_{14}$ [25] the pair of tetrahedra share the only oxygen [O(4)] of the [BaOCl] plane, because the dopant chlorine ions in the same plane do not participate in bonding. Notably, the Co-O bond length in the tetrahedral $Co(3)O_4$ unit is significantly smaller (∼1.82 Å) compared to that in all the octahedral units (1.90–1.96 Å) [12]. Also, as mentioned before, an unusual site instability around the O(4) atom is reported [16], where instead of the mean position, O(4) seems to be fractionally distributed among three sites around a threefold axis, located at the mean position.

Basic electronic structure. Considering the crystal structure given by XRD, we carried out density functional theory based spin-polarized calculations within GGA including a Hubbard on site d-d Coulomb interaction U at Co site (GGA+U). Figure 2(a) shows the spin-polarized partial density of states (pDOS) of different Co, the connected O atoms, and that of Cl. The upper left, upper right, and lower left panels in Fig. 2(a) show the pDOS projected to Co(1) d, Co(2) d, and Co(3) d states together with p states of oxygen atoms which surround the respective Co's. Focusing on the upper left panel, it shows large mixing between the octahedral Co(1) d states and the O(1) and O(2) p states which connects to Co(1). It is evident from the pDOS of the Co(1) d states that a low-spin Co state is stabilized in this case with large unoccupied up- and down-spin states. The asymmetry in the up- and down-spin oxygen states confirms the existence of spin polarization of the oxygens.

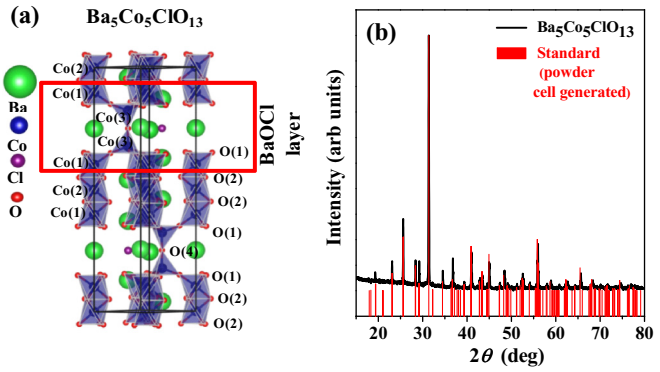

FIG. 1. (Color online) (a) Crystal structure of BCCO5. (b) Powder XRD pattern from BCCO5 matched with standard data.

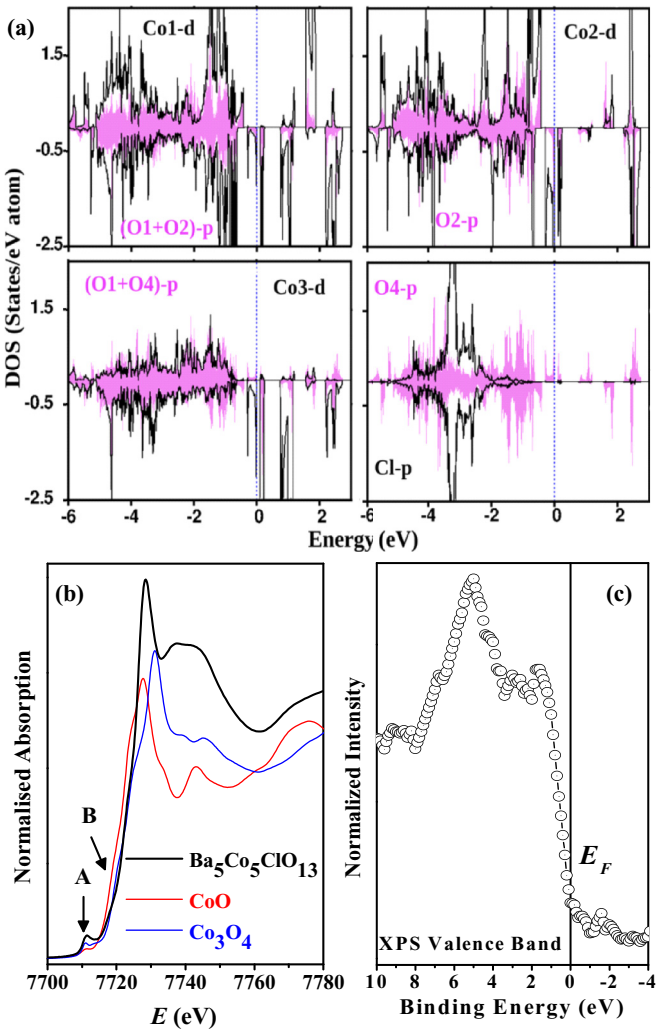

FIG. 2. (Color online) (a) GGA + U density of states, projected onto various Co-d states, as well as O-p and Cl-p states. The zero of the energy has been set at Fermi energy, E_F. (b) Normalized Co K-edge XANES spectrum from BCCO5, in comparison to CoO and Co_3O_4 spectra. (c) XPS valence band spectrum from BCCO5.

Similarly, the pDOS shown in the upper right panel confirms the low spin state of Co(2). As is evident from the plot in the lower left panel, the tetrahedral Co(3) d states are completely occupied in the up-spin channel. Thus it can be concluded that this cobalt possesses a high-spin configuration while large hole concentration on O(4) is also evident from this plot. The lower right panel shows the Cl pDOS along with that of O(4). The overlap between the Cl p-state DOS and the O(4) p-state DOS indicates the presence of certain covalent interaction between them within the BaOCl plane.

The calculated magnetic moments for Co and O sites are listed in the second column of Table I. Contrary to previously proposed Co^{4+} description [12–16], our results suggest a high-spin Co^{2+} in tetrahedral coordination (moment $\sim 3\mu_B$) with remarkably large moments on the tetrahedral oxygens, O(1) and O(4). On the other hand, Co(1) and Co(2) are in the low-spin intermediate valence state between 3+ and 4+, which would be prone to charge disproportionation, as indicated

TABLE I. Magnetic moments (in μ_B) at different inequivalent Co and O sites, and Cl site, as given by GGA+U calculation. The left (right) column represents results of calculations not taking (taking) into account the local distortion. The distortion splits O(1) and O(2) in two additional classes.

Atom	Undistorted	Distorted
Co(1)	0.329	0.321
Co(2)	2.956	2.939
Co(3)	0.504	0.983
Cl	− 0.001	0.004
O(1)	0.284	0.291
O(1)	0.284	0.251
O(2)	0.052	− 0.012
O(2)	0.052	0.012
O(4)	0.412	0.445

by the difference of magnetic moments between them. The rigorousness of these conclusions have been checked by repeating the calculations starting with different initial guesses for the spin states.

To confirm the above theoretical findings experimentally, Co K-edge XANES spectrum has been measured, as shown in Fig. 2(b). Despite the presence of many Co atoms in the cell having different valence states, the matching of experimental Co edge with that of Co_3O_4 reference (feature B in the figure) confirms the presence of Co^{2+} and other higher valent cobalt ions in BCCO5. Noticeably the preedge peak A, associated with electronic transition from s core levels to empty levels of hybridized pd states is more intense in BCCO5, suggesting higher density of empty levels in Co atoms in the system, compared to Co_3O_4. Therefore, the features of Co K-edge XANES spectrum fully support the theoretical finding regarding the Co oxidation states.

The spin-polarized GGA+U electronic structure calculation has been further carried out by considering the experimentally observed antiferromagnetic (AFM) ordering of Co spins along the c axis [14], i.e., antiparallel interaction between two adjacent ferromagnetic blocks, consisting of Co(1)-Co(2)-Co(1) octahedra and Co(4) tetrahedron. The AFM calculation resulted in an insulating solution with a small gap of 0.1 eV, which is completely consistent with the XPS valence band spectrum [Fig. 2(c)], showing zero density of states at the Fermi energy (E_F).

Local atomic structure and its implication. In order to probe the local instabilities in the unit cell, we focused on Cl ions combining Cl K-edge polarized micro-XANES (p-XANES) and quantitative EXAFS data analysis. Cl K-edge was chosen as absorption by other atoms (Ba or Co) would give only average description because of their multiple presence/valence state in the cell. As expected in the case of trigonal symmetry of the BaOCl plane [26], the Cl K-edge p-XANES spectra [cf. Figs. 4(b), 4(d), and 4(f) to be discussed later] from the single crystal BCCO5 appear identical along x and y directions, within the limit of weak noise, while the spectrum along z direction appears largely different. However, before taking up the complex modeling of these XANES spectra, it is more sensible to look at the average Cl K-edge EXAFS data collected on BCCO5 powder, as that is more suited for

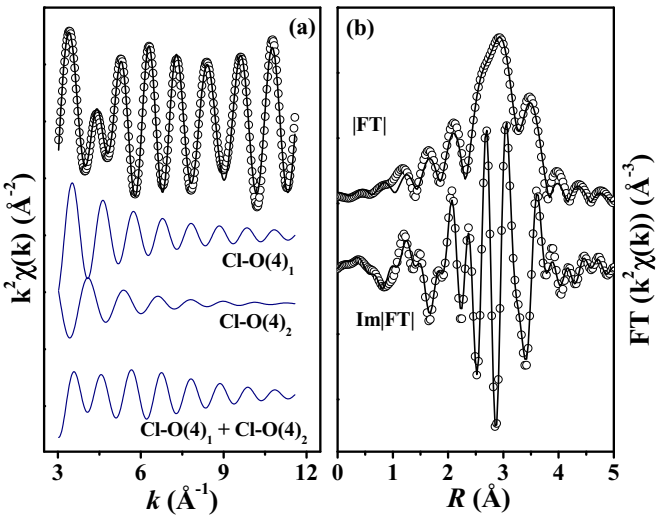

FIG. 3. (Color online) (a),(b) Experimental (points) and best fit (full line) of k^2 weighted EXAFS data and its Fourier transform moduli (|FT|) and imaginary part [Im(FT)]. The contribution of Cl-$O(4)_1$ and Cl-$O(4)_2$ shells is shown in (a).

quantitative refinement of the average local structure parameters and would provide preliminary details for interpreting the XANES region. The k^2 weighted Fourier filtered (R in between 0.5 and 4.0 Å) EXAFS signal $k^2\chi(k)$ (Fig. 3) was fitted in the k range 3–12 $Å^{-1}$ using standard procedures [27]. In order to reduce the number of free parameters and the correlation effects in the data fitting, the multiplicity numbers were kept fixed to the expected crystallographic values. The quantitative data analysis reveals interesting details (cf. Table II), i.e., in particular the Cl-O distribution appears bimodal with a closer neighbor Cl-$O(4)_1$ around 3.0 Å, characterized with larger disorder and a second shell Cl-$O(4)_2$ (two-neighbors) around ∼3.5 Å. Interestingly also the disorder is larger for in plane Cl-Ba (around 3.28 Å) with respect to the apical Cl-Ba (around 2.92 Å) shell suggesting a rather large structural disorder in the Cl-O-Ba plane. Finally, the distribution of a Cl-Co neighbor splits into two closer and four farther Cl-Co neighbors (Table II).

Next the analysis of the polarized XANES spectra were carried out considering a local cluster of 8 Å around the absorber. Specifically, the analysis of the p-XANES spectra were carried out comparing the experimental data with simulations considering different distortions of the local atomic structure around the Cl absorber. Starting from the symmetric crystallographic model, the local structure around the absorber has been progressively deformed in order to reproduce the main features of the experimental spectra. These p-XANES simulations suggest that the average trigonal symmetry is locally broken around Cl, while the overall structural symmetry is retained in average, assuming random distribution of distortions in the crystal.

TABLE II. Results of Cl K-edge EXAFS data analysis. The coordination numbers were fixed to the crystallographic values; the σ^2 of Cl-Co shells were constrained to the same value.

Shell	N	R (Å)	σ^2 ($\times 10^2$ Å^2)
Cl-Ba (apical)	2	2.92(1)	3.1(2)
Cl-$O(4)_1$	1	3.00(6)	8.0(9)
Cl-$O(4)_2$	2	3.53(2)	2.0(3)
Cl-Ba (in plane)	3	3.28(2)	14.0(2)
Cl-Co	4	3.69(2)	9.5(4)
Cl-Co	2	3.49(5)	9.5(3)

Among the many symmetry breaking possibilities, the shift of the O(4) triangle [as depicted in Figs. 4(i) and 4(j)] and the occurrence of O(4) vacancies and the associated displacement of Co(3) neighbors [as depicted in Figs. 4(k) and 4(l)] appear to be the most probable distortions that take place. The first type of distortion (C02) produces better matching of μ_{xy} with the experimental data in the white line region, and in the region around 2850 eV. On the other hand, the model presented in Figs. 4(k) and 4(l) (C44), obtained from the model C02 by removing the closer O(4) and moving the Co(3) atoms, provides some structural feature around 2850 eV, for x, y, and z directions and, in addition, shows better agreement with the experimental data in the white line region of z-direction spectrum, including the appearance of a pre-edge feature around 2825 eV. Overall, the XANES models suggest that every O(4) is shifted away (O_s in Fig. 5) from its mean position (O_m in Fig. 5) by 0.4 Å towards one of the three chlorine atoms surrounding it, each making a closely placed Cl-$O(4)_1$ pair, so that equilateral triangles of O(4) form with Cl at an off-centered position (blue triangle in Fig. 5), with one short [$O(4)_1$ at 2.85 Å] and two longer [$O(4)_2$ at 3.5 Å] Cl-O(4) arms. Such shifts of O(4) have been shown before [16,28], although those models showed only an average distribution of each O(4) atom on the three O_s positions with 1/3 occupancy. Considering the fact that the experimental time scales of both XRD and XANES experiments are comparable, this must be attributed to lack of long range order of these $ClO(4)_3$ triangles. Occasional presence of $ClO(4)_3$ isosceles triangles (orange triangle in Fig. 5) instead of the equilateral ones or the presence of oxygen vacancy (V_O in Fig. 5) in the O(4) site (see below) could be responsible for limiting the infinite growth of the ordered distortion. It should be noted here that each of these Cl-$O(4)_1$ pairs, formed due to Coulomb attraction between O(4) with hole and Cl^-, will represent an effective dipole (black arrow marks in Fig. 5). Next, the presence of V_O (vacancy) at the O(4) sites with Co(3) atoms over and below tending to collapse towards the neighboring Cl [Figs. 4(k) and 4(l)] is also motivated by Co-Cl Coulomb attraction caused by oxygen vacancy. This gives rise to an average bimodal distribution of the six nearest Co atoms around each Cl atom where two are substantially closer compared to the other four. All these distortions are in accordance with the finding of the EXAFS data (cf. Table II).

The GGA+U calculations were repeated taking into account the above distortions. The calculated moments are shown in the right column of Table I. Evidently, the distortions introduced more hole at O(4) site as well as increased the disproportionation between Co(1) and Co(2). Figure 6 shows the comparison of magnetization density shown for Co2-Co1-Co3 unit connected to the next Co3-Co1... unit via the O(4) oxygen for the structures without distortion (upper panel) and with distortion (lower panel). Most notable changes happen at the O(4) site together with change in magnetization profile

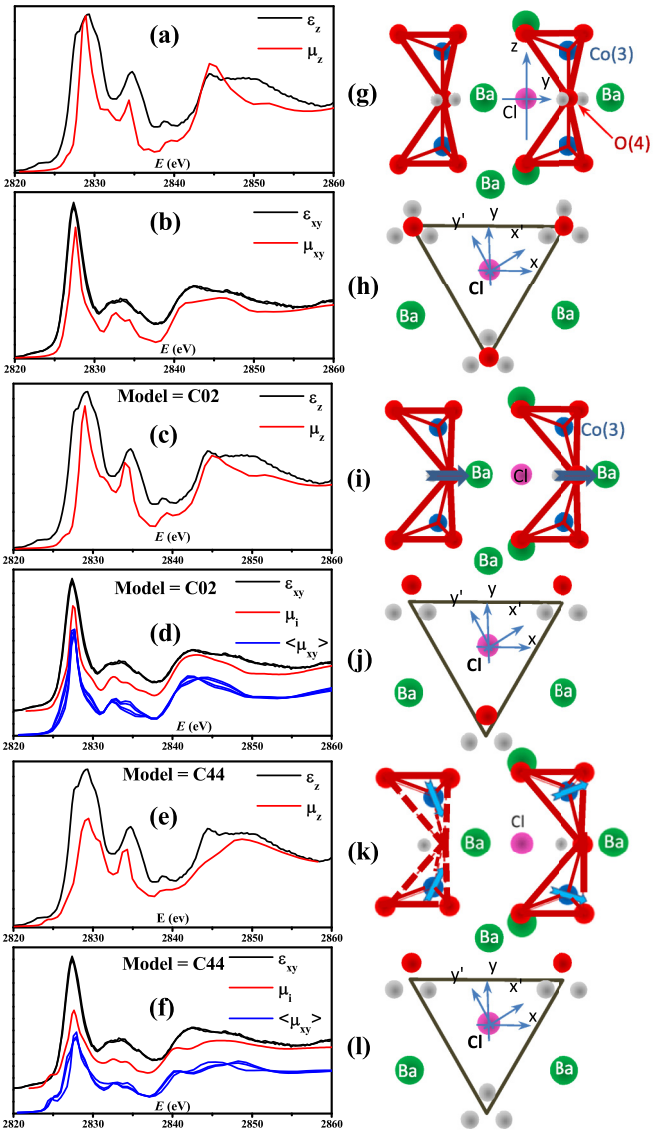

FIG. 4. (Color online) Cl K-edge XANES simulation. Each panel shows the experimental data (black) collected along z (ϵ_z, top plot), x, and y directions (ϵ_{xy}, bottom plot) compared with p-XANES models (μ_z, μ_{xy}, red curves) calculated assuming different local structure deformation as schematically represented in the right side. The symmetry breaking makes p-XANES along x, y, x', and y' different; therefore, μ_{xy} red curves are the weighted sum of the models calculated along the four possible crystal orientations. The top panels (a),(b) summarize the XANES models obtained using the crystallographic structure assuming exact trigonal symmetry of Cl local structure and O(4) located at the average positions. In the middle panels (c),(d) the O(4) atoms are located around the crystallographic positions forming an approximately equilateral triangle with a closer $O(4)_1$ and two farther $O(4)_2$ neighbors. The blue curves represent calculations obtained for independent orientation of the O(4) triangle with respect to the x-ray polarization axis. The simulations reported in the bottom panels (e),(f) are calculated assuming a vacancy in the O(4) sites associated to the distortion of Co(3) atoms: these Co(3) get closer to Cl.

located at the Co3 site (cf. encircled region). The relative strength of magnetization densities between Co1 and Co2 also change between the two structures.

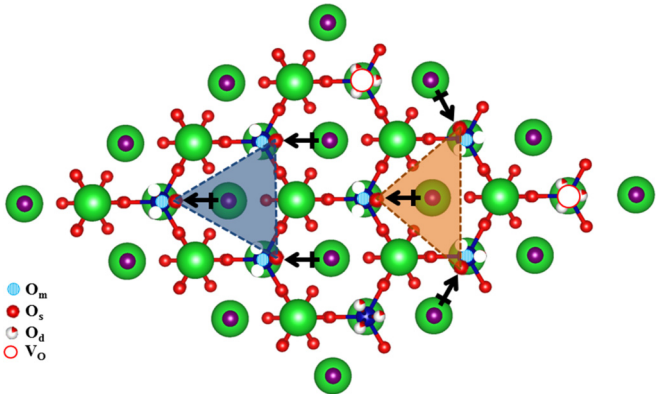

FIG. 5. (Color online) Schematics of different defects and their distributions.

Spin-phonon coupling. The above local structural analysis suggests two primary distortions/defects: (i) every O(4) moves close to one Cl forming Cl-O(4) pair [Figs. 4(i) and 4(j)] and (ii) the oxygen vacancy, promoting tilting of $Co(3)_2O(1)_6$ units towards Cl [Figs. 4(k) and 4(l)]. These distortions are expected to affect the dielectric and magnetic responses of the system. For example, the first distortion decreases the Co(3)-O(4)-Co(3) angle from 180° to ≈ 150°, which modifies the Co(3)-O(4)-Co(3) superexchange path, affecting the magnetic interaction.

Figures 7(a) and 7(b) show the temperature variation of the dielectric constant [$\epsilon(T)$] and dielectric loss ($\tan\delta$) from a BCCO5 crystal. The data exhibits a giant dielectric constant with a broad anomaly at high temperature, which drops to small value below 8–20 K, depending on the frequency. This giant dielectric constant ($\approx 10^5$) is found to be intrinsic as checked by measurements on good quality crystals, using different electrodes and contact configurations.

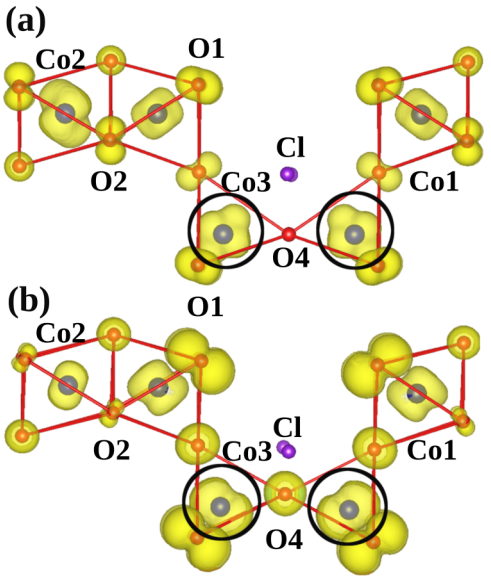

FIG. 6. (Color online) GGA+U magnetization density plots for two adjacent blocks of Co(1)-Co(2)-Co(3) units, connected through O(4), for (a) undistorted and (b) distorted crystal structures.

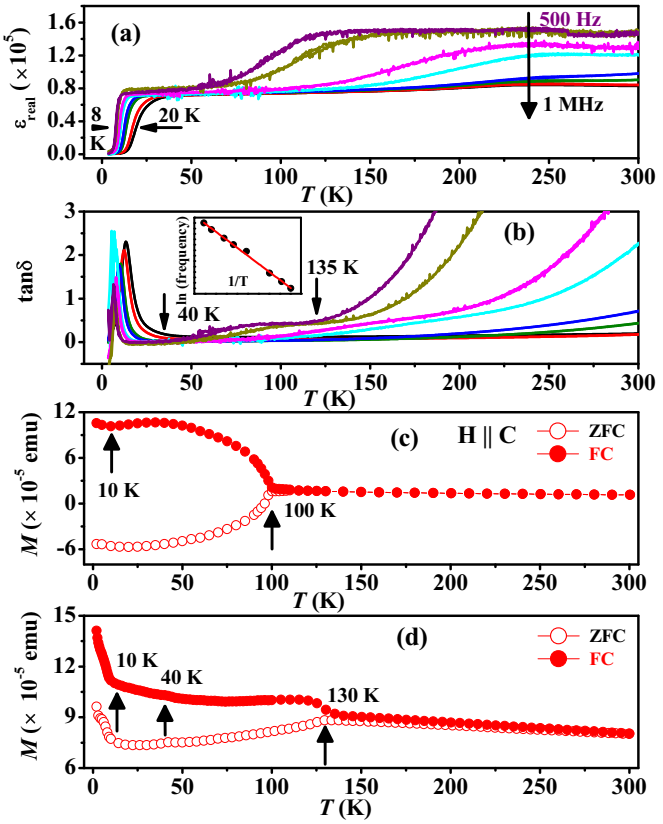

FIG. 7. (Color online) (a) Temperature variation of the dielectric constant (ϵ) data and dielectric loss (tanδ) (b) for BCCO5 crystal. Inset shows the Arrhenious fitting of the low temperature transition. (c),(d) FC-ZFC $M(T)$ data of BCCO5 crystals with 100 Oe magnetic field $\parallel c$ axis of the crystals and the same from BCCO5 polycrystalline powder.

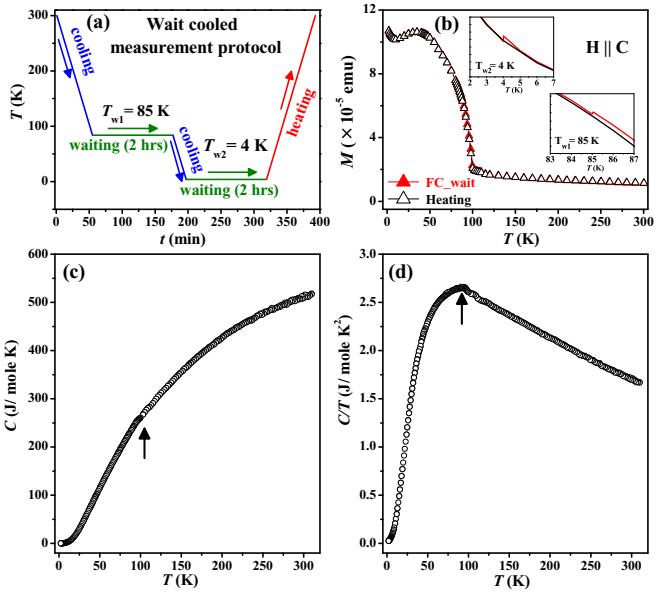

FIG. 8. (Color online) (a) Wait memory measurement protocol for $Ba_5Co_5ClO_{13}$. (b) Wait memory measurement data for $Ba_5Co_5ClO_{13}$. Inset shows the zoomed portion at the waiting temperatures. The variation of heat capacity (C) with temperature (T) is shown in (c), while C/T vs T is plotted in (d).

The anomalies in the $\epsilon(T)$ curve are manifested as a sharp peak in the tan$\delta(T)$ [Fig. 7(b)] at low temperature and a broad hump around 100 K. Both these features shift to high temperature with increasing frequencies, implying a thermally activated relaxation process. The activation energy for the low temperature transition, as estimated from the fitting [inset to Fig. 7(b)], is found to be 8.89 meV. The large dielectric constant above this transition temperature is probably related to thermally activated consolidated movements of the Cl-O(4) local dipoles in triangular fashion due to hopping of every O(4) atom within three possible sites and the alignment of these local dipoles in the presence of the electric field, while the sudden drop in dielectric constant at low temperature is related to the freezing of each O(4) atom within one particular O_s site, out of the three possibilities. The higher temperature relaxation process, starting around 40 K, is likely to be connected to similar dynamic freezing of the $Co(3)_2O(1)_6$ tilting, triggered by the presence of O(4) vacancies, towards one of the three surrounding Cl ions. However, this heavier dipole fluctuation may not be responsive to high frequency pulses and as a result this feature is observed in the $\epsilon(T)$ data only at lower frequencies.

The temperature dependence of magnetization data from single and polycrystalline BCCO5 are presented in Figs. 7(c) and 7(d). The bifurcation of the ZFC and FC curves at around 100 K parallel to the c axis and around 130 K for the polycrystalline sample signal the onset of a magnetic order, while the upturn around 10 K is related to a glassy magnetic state confirmed by magnetic memory measurement [inset to Fig. 8(b)]. The magnetic memory measurement protocol is summarized in Fig. 8(a). The ZFC-FC data from the polycrystalline sample [Fig. 7(d)] additionally shows weaker features around 40 K (see arrow). Interestingly, these features at ~10 K and ~40 K correspond to the two strong features observed in the $\epsilon(T)$ data. So, it is apparent that the process of various defect freezing makes simultaneous marks in the magnetization process by involving modulation in the magnetic superexchange path(s). The distortion due to O(4) vacancies, i.e., the tilt of the $Co(3)_2O(1)_6$ unit, probably manifests itself over larger temperature range while global freezing occurs only at ~40 K. Heat capacity measurement on aligned single crystals exhibits [Figs. 8(c) and 8(d)] only a weak feature at 100 K, while it remained featureless at lower temperatures, indicating low temperature transitions are devoid of any long range order.

The above experimental results hint towards a strong spin-phonon coupling existing in these compounds. In order to check this we calculated the Γ-point phonon spectrum, which gives the IR-active modes, and therefore contributes to the dielectric constant. We calculated phonon spectra considering ferromagnetic as well as ground state antiferromagnetic ordering of Co spins. The corresponding spectra are shown in Fig. 9. We find that the soft phonon mode gets affected by the nature of magnetic ordering, indicating the magnetostructural coupling. The examination of such phonon modes, shown as inset, reveals that it involves motion of O(4) and Cl atoms, as well as tilting motion of the $Co(3)O(1)_3$ unit. Interestingly, this also involves motion of Ba, suggesting motion in the

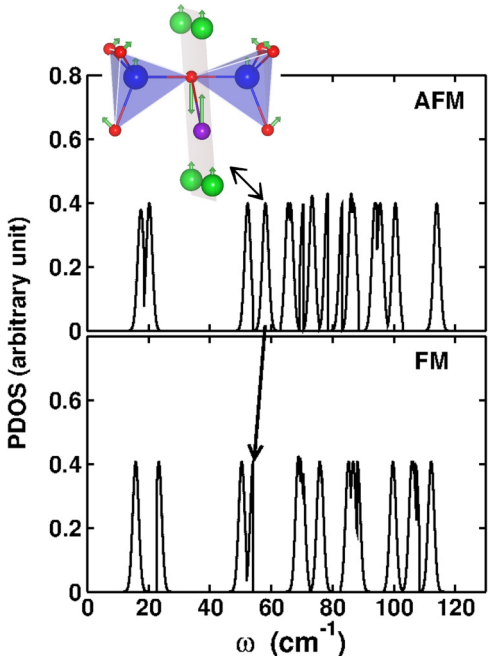

FIG. 9. (Color online) Phonon spectra of BCCO5 in FM (top panel) and AFM (bottom panel) magnetic states. The arrows show the shifting of dominant IR active phonon modes. The inset shows the displacement of atoms corresponding to one such IR-active mode.

entire BaOCl plane. This is in complete agreement with our EXAFS results (Table II) and previous investigations [17] demonstrating larger disorder in the BaOCl plane. These atomic motions affect the Co(3)-O(4)-Co(3) angle, and dictate the magnetic ground state, which suggests strong spin-phonon coupling in BCCO5, arising due to exchange striction.

IV. CONCLUSION

To conclude, irregularities, imbalance, and strong orbital overlap in a network of transition-metal ions and anions may give rise to unexpected material properties, the complete understanding of which is far from being achieved. In this study we venture into this issue, taking the example of a barium cobalt oxychloride compound, $Ba_5Co_5ClO_{13}$. Detailed structural, dielectric, and magnetic investigations as well as first-principle calculations have been carried out. Our results reveal that strong Co-O covalency in this compound causes a significant charge redistribution. The presence of a large hole concentration at the apical oxygen O(4) in the tetrahedral subunit, together with irregularities created in the anionic network through doping of Cl atoms, conspire unexpected local structural anomalies, which manifest on the dielectric and magnetic properties. The theoretical evidence of considerable spin-phonon coupling, as well as concomitant appearance of features in dielectric and magnetic properties, indicate possible existence of a large magnetocapacitance effect. Our study should motivate further investigations in this direction.

ACKNOWLEDGMENTS

S.R. thanks Council of Scientific and Industrial Research, Govt. of India and Japan Society for the Promotion of Science for funding. T.S.D. acknowledges computational facility through Thematic Unit, DST.

[1] J. Zaanen, G. A. Sawatzky, and J. W. Allen, Phys. Rev. Lett. **55**, 418 (1985).
[2] P. Olalde-Velasco, J. Jiménez-Mier, J. D. Denlinger, Z. Hussain, and W. L. Yang, Phys. Rev. B **83**, 241102(R) (2011).
[3] X. Wang, M. J. Han, L. de' Medici, H. Park, C. A. Marianetti, and A. J. Millis, Phys. Rev. B **86**, 195136 (2012).
[4] F. Reinert, S. Kumar, P. Steiner, R. Claessen, and S. Hüfner, Z. Phys. B **94**, 431 (1994).
[5] F. Reinert, P. Steiner, and S. Hüfner, J. Magn. Magn. Mater. **140-144**, 177 (1995).
[6] A. C. Stückl, C. A. Daul, and H. U. Güdel, J. Chem. Phys. **107**, 4606 (1997).
[7] D. Marabello, R. Bianchi, G. Gervasioa, and F. Cargnoni, Acta Crystallogr. A **60**, 494 (2004).
[8] R. J. Armstrong, A. H. Morrish, and G. A. Sawatzky, Phys. Lett. **23**, 414 (1966).
[9] F.-D. Tsay and L. Helmholtz, J. Chem. Phys. **50**, 2642 (1969).
[10] S.-J. Lee and S. Lee, New J. Phys. **8**, 98 (2006).
[11] P. M. Woodword, H. Mizoguchi, Y.-I. Kim, and M. W. Stoltzfus, in *Metal Oxides: Chemistry and Applications*, edited by J. L. G. Fierro (Taylor and Francis, London, 2006).
[12] K. Yamaura, D. P. Young, T. Siegrist, C. Besnard, C. Svensson, Y. Liu, and R. J. Cava, J. Solid State Chem. **158**, 175 (2001).
[13] H. Wang, J. Yang, Z. Zhang, C. Dong, and M. Fang, Phys. Lett. A **373**, 4092 (2009).
[14] M. Kauffmann, O. Mentré, A. Legris, N. Tancret, F. Abraham, and P. Roussel, Chem. Phys. Lett. **432**, 88 (2006).
[15] O. Mentré, M. Kauffmann, G. Ehora, S. D-Minaud, F. Abraham, and P. Roussel, Solid State Sci. **10**, 471 (2008).
[16] M. Kauffmann, O. Mentré, A. Legris, S. Hébert, A. Pautrat, and P. Roussel, Chem. Mater. **20**, 1741 (2008).
[17] N. Tancret, P. Roussel, and F. Abraham, J. Solid State Chem. **178**, 3066 (2005).
[18] A. L. Ankudinov, B. Ravel, J. J. Rehr, and S. D. Conradson, Phys. Rev. B **58**, 7565 (1998).
[19] G. Kresse and J. Furthmuller, Phys. Rev. B **54**, 11169 (1996).
[20] J. P. Perdew, K. Burke, and M. Ernzerhof, Phys. Rev. Lett. **77**, 3865 (1996).
[21] S. L. Dudarev, G. A. Botton, S. Y. Savrasov, C. J. Humphreys, and A. P. Sutton, Phys. Rev. B **57**, 1505 (1998).
[22] P. E. Blöchl, Phys. Rev. B **50**, 17953 (1994).
[23] P. Blaha, K. Schwartz, G. K. H. Madsen, D. Kvasnicka, and J. Luitz, in *WIEN2K, An Augmented Plane Wave + Local Orbitals Program for Calculating Crystal Properties*, edited by K. Schwarz (Technische Universitaët Wien, Austria, 2001).
[24] S. Baroni, P. Giannozzi, and A. Testa, Phys. Rev. Lett. **58**, 1861 (1987).

[25] K. Boulahya, M. Parras, J. M. Gonzalez-Calbet, U. Amador, J. L. Martinez, V. Tissen, and M. T. Fernandez-Diaz, Phys. Rev. B **71**, 144402 (2005).

[26] C. Meneghini, S. Di Matteo, C. Monesi, T. Neisius, L. Paolasini, S. Mobilio, C. R. Natoli, P. A. Metcalf, and J. M. Honig, Phys. Rev. B **72**, 033111 (2005).

[27] C. Menehgini, F. Bardelli, and S. Mobilio, Nucl. Instrum. Methods, Phys. Res. B **285**, 153 (2012).

[28] O. Mentré, H. Kabbour, G. Ehora, G. Tricot, S. D. Minaud, and M.-H. Whangbo, J. Am. Chem. Soc. **132**, 4865 (2010).